Image-based Multiscale Mechanical Analysis of Strain Amplification as a Damage Mechanism of Neurons in a Collagen Gel

Victor W. L. Chan[a], William R. Tobin[a], Sijia Zhang[b], Beth A. Winkelstein[b], Victor H. Barocas[c], Mark S. Shephard[a], Catalin R. Picu[a,d]

[a]Scientific Computational Research Center, Rensselaer Polytechnic Institute, Low Center for Industrial Innocation, CII-4011, 110 8th Street, Troy, NY 12180;
[b]Department of Bioengineering, University of Pennsylvania, 240 Skirkanich Hall, 210 South 33rd Street, Philadelphia, PA 19104;
[c]Department of Biomedical Engineering, University of Minnesota, 7-105 Nils Hasselmo Hall, 312 Church Street SE, Minneapolis, MN 55455;
[d]Department of Mechanical, Aerospace and Nuclear Engineering, Rensselaer Polytechnic Institute, Jonsson Engineering Center, Rm. 2049, 110 8th Street, Troy, NY 12180

ABSTRACT
Needs to be filled in.

1. Introduction

In early studies of tissue mechanics (reviewed in Fung's book), the focus was on developing constitutive equations that described the mechanical behavior of a tissue as a continuous, homogeneous entity. Even the continuous tissue mechanics problem is extremely difficult, with issues such as viscoelasticity [[reference]], nonlinearity [[reference]], multiphasicity [[reference]], anisotropy [[reference]], active stress generation [[reference]], damage [[reference]], and growth and remodeling [[reference]] all coming into play under various circumstances. Much of the work in the previous century of biomechanics has attempted to capture these different complexities, and this is the appropriate level at which to attack many problems given the macroscopic nature of humans and the apparent continuity of the tissue when viewed on the macro scale.

More recently, however, it has been recognized that the essential unit that responds to a macroscopic load is in fact microscopic, such as a smooth-muscle in a growing aneurysm [[reference]], a somatosensory nerve ending [[reference]], a chondrocyte remodeling the surrounding tissue [[reference]], a cell remodeling its scaffold in an engineered blood vessel [[reference]], or - most relevant to the current work - a neurite being injured by excessive stretch [[reference]]. In each of these cases, a macroscopic/tissue-scale loading condition is transferred to the microscopic/cell-scale force field, which in turn drives the response. If we hope to understand the microscopic response to a macroscopic load, a scale-bridging strategy is clearly needed.

CONTACT Catalin R. Picu. Email: picuc@rpi.edu

The constrained-mixture models (Humphrey and Rajagopal 2002) have been extremely effective in predicting growth and remodeling at the continuum scale, but they do not account for the local cell stress that arises, treating the cells instead as a continuous component of a mixture. As such, constrained-mixture models are not designed to address the effect of local strain field variations due to the presence of a cell, as observed experimentally in fibroblast-populated collagen gels [[Voytik-Harbin]]. To explore the load around a cell and to predict the forces acting on a cell, one obviously must model the cell and its surroundings as discrete entities, not as a continuous mixture.

Numerous studies have now been made using what could be broadly termed a "cell in a box" approach. Inspired by classic work in the theory of composite materials (Hashin 1962), models are constructed of a cell surrounded by acellular material, with the domain shape normally a cube or rectangle representing a small region of the tissue. In most cases [[references]], the approach employed is to place a cell of idealized shape (sphere or ellipsoid) in the center of the cube. A notable extension is the multi-cell simulations of Marquez, Genin, and Elson (Marquez et al. 2006), in which cylindrical or ellipsoidal cells were progressively added to the system, and a jump in effect was observed when the cells percolated the domain. Another important contribution (Lai et al. 2013)] was the replacement of the closed-form constitutive equation with a multiscale model that allows better representation of the extracellular matrix structure.

In spite of these recent advances, there is still considerably more work to be done in pursuing a realistic representation of the cell's (or tumor's) mechanical environment under a given tissue load. Perhaps the most salient missing feature of current models is the fact that the microscopic entity is rarely spherical in shape. A malignant tumor can have an extremely complex geometry [Cristini?], for example, and fibroblasts spread and polarize within a collagen matrix [[reference]]. There is a compelling need for methods that can account for the detailed microscale geometry when downscaling mechanical information.

[The incorporation of detailed microscale geometry entails high computational demands ...] In order to accommodate the high computational demands required to incorporate the complex neuron geometry and the multi-scale nature of the surrounding collagen gel into our model, we employ the adaptive multi-scale simulation infrastructure (AMSI) (Delalondre et al. 2010) which is designed to simultaneously handle massively parallel simulations on multiple scales.

Although the approach described herein is general, it is focused on the specific experimental system of dorsal root ganglion (DRG) neurons embedded in a collagen gel. This model system, which has been used extensively by the Winkelstein group [[reference]] and others [[reference]], allows detailed study of the cellular mechanisms of neuronal injury in a more controllable environment than can be achieved in vivo. As such, it has the potential to provide insight into the mechanism of neuronal injury under mechanical load, with biochemical markers of neuronal injury being quantified in response to different macroscopic strains and/or strain rates (Zhang et al. 2016). This system has the further advantage that it can be imaged readily via confocal microscopy, providing a 3-D image of the neurite [[reference]].

Thus, our objective in this work was to develop a general modeling strategy in which (1) confocal microscopy or another three-dimensional imaging modality is used to generate a realistic representation of a complex cell geometry, (2) that geometric model, along with the surrounding extracellular matrix, is converted to a finite-element mesh, (3) a multiscale model is implemented on that mesh using a network microstructural

model at each Gauss point (Chandran and Barocas 2007; Stylianopoulos and Barocas 2007), and (4) the solution of the mechanics problem is used to determine the distribution of strains within the cell. To test the method, we applied it to images taken of the neuron-in-gel system used by Zhang et al. (Zhang et al. 2016) [other references?] to mimic innervation of collagenous tissue. To summarize that system, dissociated dorsal root ganglion neurons were embedded in three-dimensional collagen I gels. [Sijia: anything else to say about the neuron culture?] Immunocytochemistry was performed with an antibody against the cytoskeletal protein βIII-tubulin (Abcam Cambridge, MA) to label the neuronal structure. [Also incorporate Sijia's paragraphs into introduction somewhere?]

2. Realistic Representation of Complex Cell Geometry

A realistic representation of complex cell geometry was generated from three-dimensional (3D) voxelated data that originated from a stack of image slices. Noise in the voxelated data that results from the limited level of contrast in the imaging technique are removed using a combination of erosion/dilation, manual reassignment, small object removal, and smoothing operations which were applied using the *Image-ToModel* tool (Klaas et al. 2013; Klass Ottmar 2014; sim 2017). Once processed, the voxelated data is converted into a discrete geometry via an initial triangulation that is based on voxel level operations where mesh coarsening is not performed until after the surface triangulation has been smoothed (Klaas et al. 2013). Quantization artifacts on the surface of the geometry due to the voxel nature of the data are removed using a smoothing algorithm that consists of three steps (Klaas et al. 2013): (i) calculate the surface normal of the desired surface geometry at each mesh face based on the normals of neighboring mesh faces; (ii) smooth surface normals on mesh to obtain the normals of desired surface geometry; (iii) iteratively adjust the mesh vertex positions to create a surface that matches the smoothed surface normals.

In this work, the input 3D voxelated data originated from a stack of confocal images of the neuron-in-gel system. Immunocytochemistry was performed with an antibody against the cytoskeletal protein βIII-tubulin (Abcam Cambridge, MA) to label the neuronal structure. Z-stack Images (2-micron thick) were taken by a Zeiss LSM 510 confocal microscope (Carl Zeiss Inc., Thornwood, NY) using a 40X objective and with a resolution of 0.22 micron/pixel. Images from the Z-stack are shown in Fig. 1
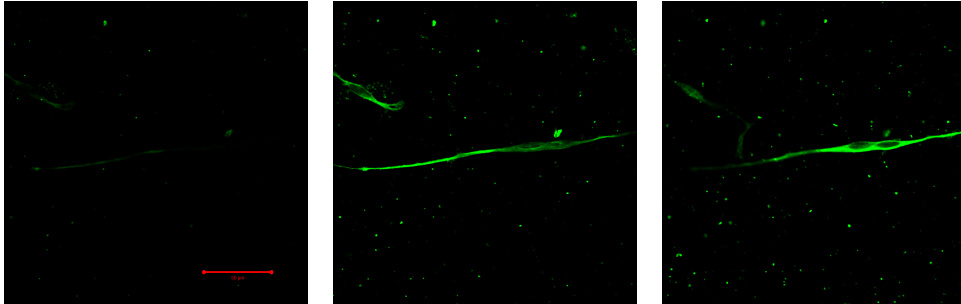
Figure 1. Images taken from Zeiss LSM 510 confocal microscope. The scale bar for 50μm is shown in the left image.

The confocal images were stacked together and converted to a 3D voxelated data set using *ImageJ* (Schneider et al. 2012), where each voxel has dimensions of 0.22μm

$\times\ 0.22\mu$m $\times\ 2\mu$m. Subsequently, the discrete geometry generated from the voxelated neuron-in-gel data was enclosed in a box that represents the domain of the collagen gel, where the neuron-gel interface is perfectly bonded. A mesh of 82,105 tetrahedral elements was generated on the non-manifold neuron-in-gel geometry using the SimModeler tool of Simmetrix Inc. (sim 2017; Shephard 2000). The neuron-in-gel voxelated data, discrete geometry, and corresponding mesh are shown in Figs. 2(a) - (c), respectively.

(a) $\qquad\qquad\qquad\qquad$ (b) $\qquad\qquad\qquad\qquad$ (c)
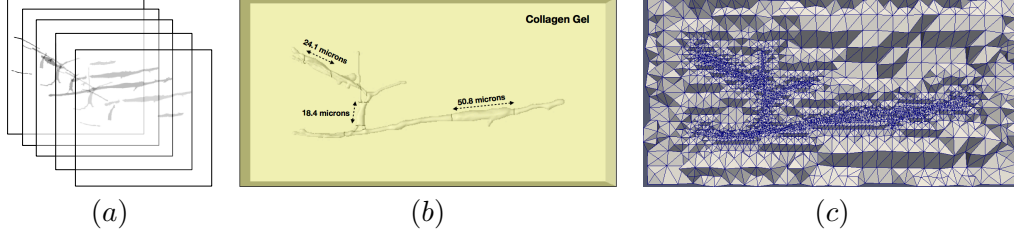
Figure 2. (a) Stack of confocal images of neurons from Fig. 1. (b) Geometric model of neurons that are embedded in collagen gel. The embedded-neuron geometry was generated using the *ImageToModel* tool (Klaas et al. 2013; Klass Ottmar 2014; sim 2017) from Simmetrix Inc. The neuron cell bodies are labeled with their axial length - axons are unlabeled. The region enclosing the neurons is the collagen gel. (c) Cut in neuron-in-gel model showing the mesh generated using the SimModeler tool (sim 2017; Shephard 2000) from Simmetrix Inc. A mesh of 82,105 tetrahedral elements is used for simulations in this work.

3.   Multi-Scale Method for Modeling Collagen Gel

Collagen gels have been modeled in the past using a multi-scale formulation based on volume averaging of fiber-network representative volume elements (RVEs) (Chandran and Barocas 2007; Stylianopoulos and Barocas 2007; Barocas 2007; Lai et al. 2012; Lake et al. 2012). Such a multi-scale formulation is also employed in this study to model the collagen gel surrounding the neurons. The multi-scale formulation consists of two scales: the microscopic scale that represents the fiber level and the macroscopic scale that represents the tissue level. Quantities corresponding to the microscopic and macroscopic scales are denoted with (m) and (M) superscripts, respectively. The Einstein summation convention is applied only to subscripts i, j, and k.

The microscopic scale is represented by a fiber network, which defines the RVE. Each RVE is generated from the Delaunay triangulation of randomly placed seed points - the edges of the triangulation represent the fibers of the network. Each fiber only carries an axial load with the axial force given by:

$$T^{(m)} = \begin{cases} \frac{E_f A_f}{B}\left[\exp\left(0.5B(\lambda_f^2 - 1)\right) - 1\right] & \text{if } \lambda_C \leq \lambda_f \leq \lambda_S \\ H_C\lambda_f + h_C & \text{if } \lambda_f < \lambda_C \\ H_S\lambda_f + h_S & \text{if } \lambda_f > \lambda_S \end{cases} \qquad (1)$$

where

E_f : linear modulus of a collagen fiber.

A_f : cross-sectional area of fiber.

B : constant parameter that controls nonlinearity.

$\lambda_f \equiv \dfrac{l}{l_0}$ where l and l_0 are the current and initial lengths, respectively, of the fiber.

λ_S : fiber stretch value at which the fiber relation transitions from nonlinear to linear.

λ_C : fiber compression value at which the fiber relationship transitions from nonlinear to linear.

$H_n \equiv E_f A_f \lambda_n \exp\big(0.5B(\lambda_n^2 - 1)\big)$ for $n = S$ or C.

$h_n \equiv \dfrac{E_f A_f}{B} \big[\exp\big(0.5B(\lambda_n^2 - 1)\big) - 1\big] - H_n \lambda_n$ for $n = S$ or C.

The fiber force shown in Eq. (1) transitions from a nonlinear to linear relationship when the fiber is stretched beyond λ_S or compressed below λ_C. The transition to a linear fiber force relationship for large fiber stretch in tension is consistent with experimental measurements of single fibers (Eppell et al. 2006; Svensson et al. 2010). In principle, fibers do not carry load in compression. Since the fibers in this model only have axial forces, the stiffness in compression was chosen to be significantly smaller than that in tension to mimic buckling.

In order to solve for network equilibrium in the RVE, displacement boundary conditions are imposed. The displacements at the corners of the RVE are dictated by the deformation state of the macroscopic scale via

$$u_i^{(c,m)} = (F_{ij}^{(M)} - \delta_{ij})\frac{x_j^{(c,m)}}{L^{(m)}}, \tag{2}$$

where $F_{ij}^{(M)}$ is the deformation gradient tensor of the macroscopic scale, $u^{(c,m)}$ are the displacements at the corners of the RVE, and $x^{(c,m)}/L^{(m)}$ are the coordinates at the corners of the RVE. In Eq. (2), $x_j^{(c,m)}$ are coordinates of a dimensionless computational domain that is a cube spanning the domain defined by (-0.5,0.5) in each of the coordinate axes. The scale conversion, $1/L^{(m)}$, relates the unit lengths between the computational and physical domains. It is important to note that Eq. (2) is valid because the center of the RVE is defined at the origin of the computational domain. The boundary displacements on each node lying on the boundary of the RVE are determined via linear interpolation.

Upon solving for network equilibrium in each RVE, the volume-averaged Cauchy stress tensor of the microscopic scale is computed from the forces acting on nodes that lie on the boundary of the RVE (bcl) (Chandran and Barocas 2007; Stylianopoulos and Barocas 2007)

$$s_{ij}^{(m)} = \frac{1}{V^{(m)}} \sum_{\text{bcl}} x_i^{(m)} T_j^{(m)}, \tag{3}$$

where $V^{(m)}$ is the current volume of the RVE, $T_j^{(m)}$ is the jth component of the fiber force, and $s_{ij}^{(m)}$ are elements of the microscopic stress tensor. The microscopic

stress tensor is transformed to the macroscopic stress tensor by rescaling by $L^{(m)}$. This procedure is needed due to the difference in length scales between the physical macroscopic domain and the non dimensional microscopic computational domain. The macroscopic Cauchy stress tensor is determined from scaling $s_{ij}^{(m)}$ by

$$\sigma_{ij}^{(M)} = s_{ij}^{(m)} \left(\frac{1}{L^{(m)}} \right)^2. \tag{4}$$

The Cauchy stress tensor obtained from the microscopic scale is used to solve the macroscopic force balance (Chandran and Barocas 2007; Stylianopoulos and Barocas 2007)

$$\sigma_{ij,i}^{(M)} = \frac{1}{V^{(m)}} \int_{\partial V^{(m)}} \left(s_{ij}^{(m)} - \sigma_{ij}^{(M)} \right) u_{k,i}^{(m)} n_k dA^{(m)}, \tag{5}$$

where $u_k^{(m)}$ is the displacement of the RVE boundary on the microscale and n_k is the unit normal vector. The right-hand side of Eq. (5) acts as a body force that accounts for the correlation between the inhomogeneous displacement of the RVE boundary and local inhomogeneities in the stress field(Chandran and Barocas 2007; Stylianopoulos and Barocas 2007). Equation (5) arises from integration of the microscopic-scale (RVE) Cauchy stress balance, $\sigma_{ij,i}^{(m)} = 0$. If the RVE did not deform, then the averaged equation would just be $\sigma_{ij,i}^{(M)} = 0$. When the RVE deforms, however, and that deformation is position-dependent, then the average of the divergence of the stress ($\sigma_{ij,i}^{(m)}$) is no longer equal to the divergence of the average stress ($\sigma_{ij,i}^{(M)}$), and a correction term must be introduced, analogous to the corresponding term in the Reynolds transport theorem (Whitaker 1999). The right-hand side of Eq. (5) is that correction and accounts for the correlation between RVE stress and boundary displacement.

The scaling parameter between the computational and physical domains, L, in Eqs. (2) and (4) is required for both the downscaling and upscaling procedures. It is determined by comparing the average fiber length in the RVEs to that in reconstituted collagen type I networks (Lindström et al. 2013) with collagen concentration of 2mg/mL, the concentration used in (Zhang et al. 2016). In the computational domain, fiber networks have a network density (total length of fibers/RVE volume) of 100 ($\pm$ 1) and an average fiber length of 0.26. The average fiber length in reconstituted collagen type I networks is 1.81 μm (Lindström et al. 2013). Based on these average lengths, $L = 7$ μm.

4. Constitutive Relationship for Modeling of Neurons

Cross-linked axially-aligned microtubule bundles are a major structural feature of axons and give rise to macroscopic anisotropic mechanical behavior (Peter and Mofrad 2012). To account for such mechanical anisotropy, the axons are modeled as a transversely isotropic hyperelastic material (Bonet and Wood D 2008; Bonet and Burton 1998). The elements of the Cauchy stress tensor and spatial (Eulerian) elasticity tensor are expressed in terms of neo-Hookean (nh) and transversely isotropic (trns) compo-

nents (Bonet and Burton 1998)

$$\sigma_{ij} = \sigma_{ij}^{\text{nh}} + \sigma_{ij}^{\text{trns}} \quad \text{and} \quad c_{ijkl} = c_{ijkl}^{\text{nh}} + c_{ijkl}^{\text{trns}}, \tag{6}$$

respectively, where

$$\sigma_{ij}^{\text{nh}} = \frac{\mu}{J}(b_{ij} - \delta_{ij}) + \lambda(J-1)\delta_{ij}$$

$$\sigma_{ij}^{\text{trns}} = \frac{2\beta}{J}(a_r a_r - 1)\delta_{ij} + \frac{2}{J}[\alpha + 2\beta \ln J + 2\gamma(a_r a_r - 1)]a_i a_j - \frac{\alpha}{J}(b_{is}a_s a_j + a_i b_{jr}a_r)$$

$$c_{ijkl}^{\text{nh}} = \lambda(2J-1)\delta_{ij}\delta_{kl} + \frac{2}{J}[\mu - \lambda J(2J-1)]\delta_{ik}\delta_{jl}$$

$$c_{ijkl}^{\text{trns}} = \frac{8\gamma}{J}a_i a_j a_k a_l + \frac{4\beta}{J}(a_i a_j \delta_{kl} + \delta_{ij}a_k a_l) - \frac{\alpha}{J}(a_i a_l b_{jk} + b_{ik}a_j a_l) - \frac{4\beta}{J}(a_r a_r - 1)\delta_{ik}\delta_{jl}. \tag{7}$$

In Eq. (7), b_{ij} are elements of the left Cauchy-Green strain tensor and a_i is a component of the mapping of the direction of anisotropy in the undeformed state to the current state via the deformation gradient. In tensor notation, $\boldsymbol{a} \equiv \boldsymbol{FA}$, where $\boldsymbol{A}$ is the direction of aniostropy in the undeformed state and $\boldsymbol{F}$ is the deformation gradient tensor. λ and μ are the Lamé constants that define the material properties of the isotropic component, while β, γ, and α are parameters that define the material properties of the anisotropic component. The parameters of Eq. (7) can be written in terms of material constants as

$$\lambda = \frac{2\mu(\nu + n\nu^2)}{m} \qquad \gamma = \frac{E_A(1-\nu)}{8m} - \frac{\lambda + 2\mu}{8} + \frac{\alpha}{2} - \beta$$

$$\alpha = \mu - G_A \qquad m = 1 - \nu - 2n\nu^2$$

$$\beta = \frac{\mu\nu^2(1-n)}{2m} \qquad n = \frac{E_A}{2\mu(1+\nu)}, \tag{8}$$

where μ is the shear modulus, G_A is the axial shear modulus, ν is the Poisson ratio, and E_A is axial Young's modulus. In our analysis, the shear modulus is set to be isotropic such that $G_A = \mu$ and $\alpha = 0$. All the constants in Eq. (8) are set once all material constants (μ, G_A, ν, and E_A) are specified.

5. Parameter Specifications

5.1. Multiscale Model for Collagen Gel

The parameters for the multiscale model are listed in Table 1. The value of A_f was chosen according to Ref. 7 where the fiber radius of rat tail collagen I was measured to be 162 nm. All other parameters for the fiber-force relationship in Eq. (1) were chosen to obtain a good fit to an experimental stress-strain curve. To obtain the stress-strain responses experimentally, collagen I gels were subjected to uniaxial tensile loading at 0.5mm/s to 8mm (25% strain) using an Instron 5865 (Instron, Norwood, MA), as described in Zhang et al. (2016). The Instron Bluehill software collected the force and displacement data at 1kHz during loading. The stress and strain data were subsequently determined from the force and displacement data by dividing by the initial cross-sectional area and length, respectively, of the sample.

Parameter	Specification	Source
E_f	200 kPa	Fit to experimental data.
A_f	82.5 μm^2	Based on Dutov et al. (2016)
B	20	Fit to experimental data.
λ_S	1.13	Fit to experimental data.
λ_C	1.0	Chosen to mimic buckling.
H_S	297.25 μN	From above parameters.
H_C	16.5μN	From above parameters.
h_S	-322.74 μN	From above parameters.
h_C	-15.67μN	From above parameters.
$L^{(m)}$	7 μm	Based on Lindström et al. (2013). See Section 3.

Table 1. Parameters for multiscale model of collagen gel.

The stiffness in tension and compression in the linear regimes of the fiber force are 29.7 kPa and 1.65 kPa, respectively, for the values listed in Table 1. The fiber force is plotted in Fig. 3(a). As mentioned above, the significantly smaller stiffness in compression relative to tension was chosen to mimic buckling of the fiber. The stress-strain curves calculated from simulation using the parameters in Table 1 and measured experimentally are shown in Fig. 3(b).

For the parameters in Table 1, the Poisson ratio and fiber alignment were also examined. Experimentally, the Poisson ratio was measured by [... Sijia: can you describe how Poisson ratio was measured here?] Computationally, the Poisson ratio was determined from the volume change of the domain via

$$\nu = \frac{1}{2}\left(1 - \frac{\Delta V}{V_0}\frac{l_0}{\Delta l}\right). \tag{9}$$

Equation 9 is a conventional measure of contraction that is derived from the usual definition of volumetric strain. Although Eq. (9) is derived for small strain deformation, we conventionally extend the definition to the present case. The Poisson ratio as a function of the bulk strain is plotted in Fig. 3(c).

As seen in Fig. 3(c), the Poisson ratio calculated from simulation does not increase as drastically as that measured experimentally. Nonetheless, the Poisson ratio does increase as a function of applied strain, and becomes larger than 0.5 at an applied strain of approximately 17%. The increasing Poisson ratio at larger applied strains is due to the presence of free volume in the network which allows significant geometric reorganization and fiber alignment (Vader et al. 2009). At lower strains, the increasing Poisson ratio is due to nonlinearity of the network kinematics.

Fiber alignment is measured using the orientation index P_2. The value of P_2 is calculated from the angle θ between fibers and the direction of alignment

$$P_2 = \frac{3 < \cos^2\theta > -1}{2}, \tag{10}$$

where $< x >$ denotes the average of x over all fibers. The value of P_2 ranges from 1 ($\theta = 0$ or π) in which the fibers are completely aligned to -1/2 ($\theta = \pi/2$) in which the fibers are orthogonal to the alignment direction. When $P_2 = 0$, the fiber network is randomly oriented.
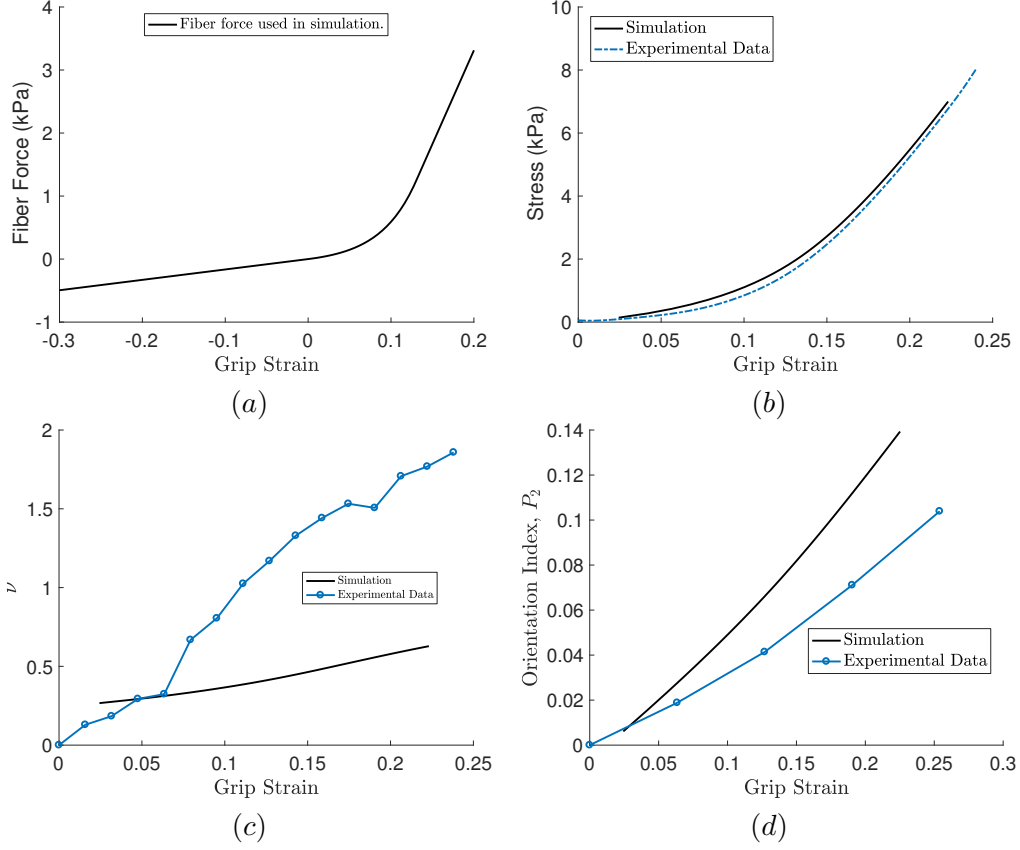
Figure 3. Plots of (a) Fiber force, (b) stress-strain curve, (c) Poisson ratio, and (d) fiber aligment metric P_2 for parameters listed in Table 1. Results from simulation plotted using black solid line, while experimentally measured data are plotted in blue dotted or blue dash-dotted lines.

Experimentally, the fiber alignment in innervated collagenous tissue was measured using the Quantitative Polarized Light Imaging (QPLI) method (Quinn and Winkelstein 2008, 2009) where alignment angle α and retardation δ is measured in each pixel. Our customized QPLI system (Zhang et al. 2016) is comprised of a fiber-optic light source (Dolan-Jenner Industries Inc., Boxborough, MA), a motor-controlled linear polarizer (Edmund Optics, Barrington, NJ) that rotates at 750 rpm, and a circular analyzer mounted to a high-speed camera (Phantom-v9.1; Vision Research Inc, Wayne, NJ) (Zhang et al. 2016). The QPLI system was integrated with the mechanical testing device, and collagen I gels were placed between the rotating polarizer and the circular analyzer. Polarized light images were acquired during tensile loading at 500 fps with 14.5 pixel/mm resolution and processed using harmonic analysis to extract the alignment angle and retardation (Tower et al. 2002; Quinn and Winkelstein 2008). The orientation index P_2 is calculated from α and δ of the QPLI method via (see Appendix A for derivation)

$$P_2 = \frac{1}{2}\left(3\int_0^\pi p(\theta)\cos^2\theta d\theta - 1\right)$$

$$p(\theta) = \frac{1}{N}\sum_{i=1}^N \left[\frac{1-2\delta_i}{\pi} + \frac{4\delta_i}{\pi}\cos^2(\theta-\alpha_i)\right], \tag{11}$$

9

where δ_i and α_i are the retardation and alignment angle, respectively, of the ith pixel. The fiber alignment as a function of bulk applied strain calculated from simulation and measured experimentally are plotted in Fig. 3(d). [How to explain discrepancy in alignment between simulation and experiments?]

[Although the alignment and Poisson ratio do not match well, the general behavior in these two properties is captured. The choice of our parameters was based on stress-strain.]

5.2.   Constitutive Relationship for Neuron

The value of E_A in Eq. (8) is based on the study by Peter and Mofrad (Peter and Mofrad 2012), where the mechanical behavior of axonal microtubule bundles under tension was simulated with a discrete bead-spring model. To apply their results for microtubule bundles to our neuron model, we assume that only the microtubule bundles carry force in the axon and that the stress of the microtubule bundles can be redistributed over the cross-sectional area of the axon. Since the microtubules are the stiffest component of the cytoskeleton (Fletcher and Mullins 2010), the mechanical contribution from the actin filaments (membrane cortex) is ignored. Based on these assumptions, the axial stiffness of the axon can be related to the axial stiffness of the microtubule bundles, E_{MTb}, by

$$E_A = \frac{E_{MTb}A_{MTb}}{A_A}, \tag{12}$$

where A_{MTb} and A_A are the cross-sectional areas of the microtubule bundle and axon, respectively. Peter and Mofrad (Peter and Mofrad 2012) suggested that the stress-strain relationship of the microtubule bundle is well represented by a power-law fit that results in a strain-dependent elastic modulus. For this study, E_{MTb} was taken to be an average value of [6.7×10^6 kPa (4×10^4 kPa used before)] and the tangent stiffness is nearly constant with a value of 4×10^5 GPa [I think better to show ranges of values. Show power fit of stress-strain curve]. The value of A_{MTb} was determined to be 0.0344 μm^2 from the hexagonal bundle geometry of the microtubules (see Ref. (Peter and Mofrad 2012) for schematic). The cross-section of the hexagonal bundle contains 19 rows of microtubules with a center-to-center microtubule spacing of 45nm. Each individual microtubule has a diameter of 25nm. The value of A_A was determined to be 19.6 μm^2, based on an average axon diameter of 5 μm in the neuron structure. From the above values, E_A is determined from Eq. (12) to be [12 MPa (70 kPa used before)].

The parameters used in Eq. (8) for modeling the neuron structure are listed in Table 2. The transverse stiffness of the axons and cell bodies was based on the measurements of Simon et al. (Simon et al. 2016) and chosen to be 1.5 kPa. The six constants in Eq. (8) are all determined when the values listed in Table 2 are fully specified.

Lastly, the axial stiffness of the cell body was chosen based on the relative alignment of the microtubules. The microtubules transition from an aligned state in the axon to an unaligned state within the cell body [Sijia, Beth, Victor B.: Do you know of any reference to describe/justify this?], where a cell-body/axon interface is defined as the starting point for the unaligned state of the microtubules. Within the cell body, the microtubules become progressively less aligned with the center of the cell body having the least alignment. Consequently, the axial stiffness within the cell body decreases and is lowest at the center. To capture such behavior, the cell bodies are also modeled

Parameter	Specification	Source
E_A	[12 MPa (70 kPa used before)]	Calculated from Eq. (12).
E_T	1.5 kPa	Based on Simon et al. (2016)
ν	0.3	[How was Poisson ratio chosen?].
μ	0.577 kPa	Calculated from E_T and ν.
$G_A(=\mu)$	0.577 kPa	Shear modulus assumed to be isotropic.
n	[46.7]	Calculated from E_A, μ, and ν.
m	-7.7	Calculated from ν and n.
λ	-0.67 kPa	Calculated from ν, μ, n, and m.
α	0 kPa	Calculated from μ and G_A.
β	0.154 kPa	Calculated from μ, ν, n, and m.
γ	[-1.01 kPa]	Calculated from E_A, ν, m, λ, μ, α, and β.

Table 2. Parameters for constitutive model of neuron.

as a transversely isotropic hyperelastic material where the axial stiffness is a function of distance from the cell-body/axon interface by

$$E_A^{cell} = \left(1 - \frac{D}{t}\right) E_A. \qquad (13)$$

In Eq. (13) D is the distance of an interior point of the cell body to the closest cell-body/axon interface and t is a constant that dictates how quickly E_A decreases when moving from the cell-body/axon interface towards the interior of the cell body. The axial stiffness decreases more quickly for smaller values of t. According to Eq. (13), E_A^{cell} depends on D, which is the nearest distance from the cell-body/axon interface. As seen in Fig. 2(b), the largest cell body in the neuron structure has an axial length of approximately 51 μm, which gives a maximum D value of 25.5 μm. The axial stiffness in the neuron structure for $t = 30\mu$m and $E_A =$[12 MPa (70 kPa used before)] is shown in Fig. 4
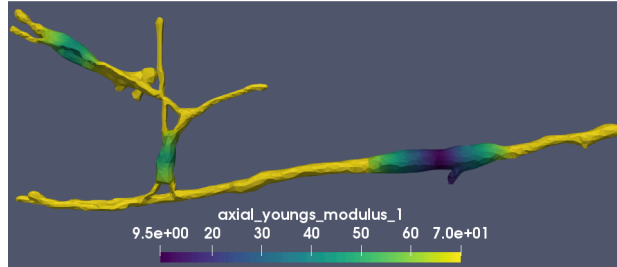
**Figure 4.** Plot of axial Young's modulus for $t = 30\mu$m in Eq. (13) and $E_A = 70$ kPa.

6. Implementation

6.1. Multi-scale

Our multi-scale model is implemented using the adaptive multi-scale simulation infrastructure (AMSI) (**?**), which is designed to support massively parallel simulations on

11

multiple scales. AMSI accommodates the computational demands of the multi-scale simulation by combining existing single-scale analysis codes into multi-scale analyses.

The macroscopic simulation code and the microscopic simulation codes are decoupled save for their interactions through the AMSI libraries. AMSI manages the parallel execution space for each code, as well as the parallel communication required for the transmission of required data between the scales. Each of the scales in the simulation supplies information required to inform the requirements of the multi-scale communication and the distribution of inter-scale coupling data in both the parallel execution space and the problem domain. This data is used by the AMSI multi-scale systems to communicate the coupling data required at each phase of simulation, and accommodate dynamic run-time operations such as load balancing while maintaining the coupling communication model. A discussion of the underlying design considerations of AMSI can be found in (Delalondre et al. 2010).
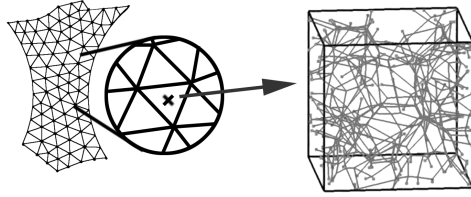
Figure 5. Schematic showing the hierarchy of scales in the multi-scale simulation

The macroscopic continuum and microscopic fiber network simulation physical scales are assumed to be strongly separated allowing the application of well-defined domain relationships between the scales. Thus no runtime considerations are required with respect to domain data locality. Parallel data locality of the required coupling data must still be accounted for during simulation execution.

The macro-scale domain is discretized using an unstructured mesh that is partitioned across the parallel execution space of the scale. Figure 5 depicts the relationship between the two scales with respect to the macro-scale unstructured mesh, an individual numerical integration point on that mesh, and the RVE-level microscale simulation corresponding to that macro-scale location.

AMSI models the relationship between the domains of the macro-scale and microscale problem. [This model combined with a model of the parallel distribution the data structures modeling the domains of each scale and the physical quantities relevant to a particular multi-scale coupling allow the construction of a parallel communication plan used to link coupling data between scales over the course of a simulation. (confusing. sentence too long.)] Up- and down-scaling transformations of the coupling data currently take place in user code after (or before) employing the [communication plane (the concept of a "communication plane" is unclear)].

At each macro-scale numerical integration point, the deformation gradient $\boldsymbol{F}$ is calculated and provided to the AMSI coupling system, which uses a communication plan to provide the value to the micro-scale RVE simulation related to the integration point. This value is used by the micro-scale as shown in Eq. (2) to establish the boundary conditions for the current state of the micro-scale RVE problem. Once a solution has been reached for the micro-scale simulation, the macro-scale stress term

12

$\sigma^{(M)}$ from Eq. (4) and the macro-scale stress divergence term $\nabla \cdot \sigma^{(M)}$ from Eq. (5) are supplied to AMSI. These terms are communicated to the macro-scale and associated with the coupled integration point for use in assembling the macro-scale linear algebraic system for the current Newton iteration.

6.2. Problem Specification

The solution to the macroscopic boundary value problem in Eq. (5) is obtained using the Finite Element method (FEM) (Bonet and Wood D 2008). The domain of the embedded neuron is discretized by a mesh consisting of 82,105 linear tetrahedral elements - 14,250 in the neuron and 67,855 in the collagen gel - giving rise to more than 985k degrees of freedom (DOF) for the macroscopic scale.

The computation demands are substantially greater for the microscopic scale where each fiber network RVE consists of, on average, 284 fiber cross links with three DOF, giving rise to 852 DOF per RVE. Since there is a single RVE for each numerical integration point of the macroscopic mesh of the collagen gel, the total DOF for the microscopic scale is more than 57 million (852 DOF/RVE × 67,855 RVEs).

Clearly, the bulk of the computational demand lies at the microscopic scale. Combined, a total of XXX DOF must be solved per loading step in our calculations. To solver our problem we use 128 macroscale processors and 1920 microscale processors.

7.   Methods

7.1. Strain Quantification

The strain within the neuron is quantified by a complementary cumulative distribution function (ccdf) defined as

$$\text{ccdf}(X) = \int_X^\infty p_{\epsilon^*}(X) d\epsilon^* = \Pr[\epsilon^* \geq X], \tag{14}$$

where $p_{\epsilon^*}(X)$ is the probability density function of ϵ^* and ϵ^* is either the axial, ϵ_{axial}, or transverse, $\epsilon_{\text{transverse}}$, strain with respect to the local axon axis. Equation 14 is the probability that the neuron structure (equivalent to the volume fraction of the neuron) experiences an axial or transverse strain of *at least X*.

7.2. Loading Direction

Three loading directions corresponding to 0, 45, and 90 degrees are considered. The three loading directions are schematically illustrated in Fig. 6. When the loading direction on the collagen gel is varied, the structural features in the neuron are exposed to different modes of deformation. Therefore, by examining different loading directions, we are able to develop insights about how the strain distribution in the neuron depends on its mechanical environment.

7.3. Choice of Axial Stiffness in the Cell Body

The transition in the axial stiffness of the cell bodies presented in Eq. (13) is artificial. To understand how this transition affects the final strain distribution in the neuron,
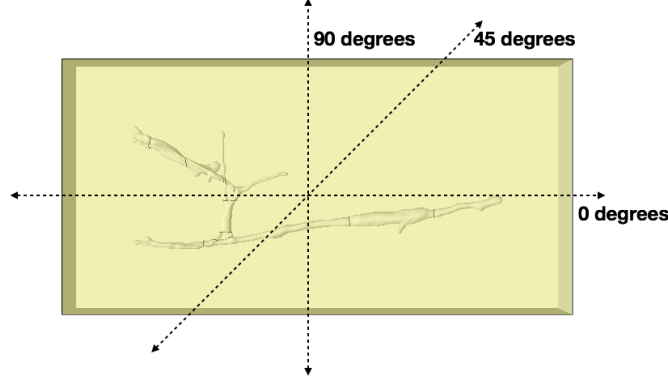
Figure 6. Schematic showing axes of load directions corresponding to 0, 45, and 90 degrees.

the transition rate is varied by adjusting t in Eq. (13). As seen from Eq. (13), the value of t needs to be greater than D (=25.5 μm) in order for E_A^{cell} to be positive. Consequently, three values of t are considered: $t = 28$ μm, 30 μm, and 50 μm, which correspond to axial stiffnesses of approximately 6.25 kPa, 10.5 kPa, and 34.3 kPa, respectively, at the center of the largest cell body in the neuron structure. The ccdfs for different axial stiffnesses of the cell body (different values of t) are plotted in Fig. 7 for the 0 degree loading case for a grip strain of 16% on the collagen gel.

(a) $\qquad\qquad\qquad\qquad\qquad$ (b)
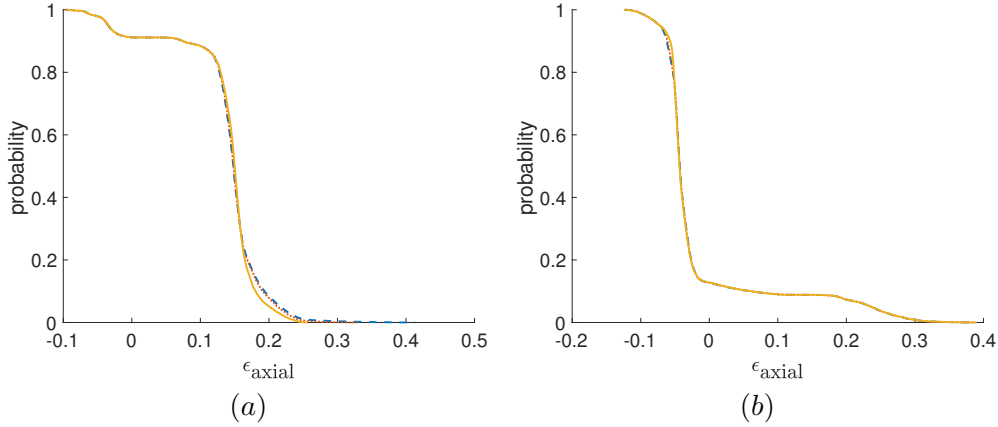
Figure 7. Complimentary cumulative distribution functions for (a) axial and (b) transverse strains in the neuron due to 0 degree load of 16% grip strain. The distributions are for axial cell-body stiffnesses corresponding to t=28 (blue dashed line), 30 (red dotted line), and 50 (yellow solid line).

As seen in Fig. 7, a small decrease in the axial strain is detected when E_A^{cell} increases from 6.25 kPa to 34.3 kPa for $\epsilon_{\text{axial}} > 0.15$. For transverse strain the distributions are nearly identical for all cell body stiffnesses considered. These results suggest that the strain distribution within the neuron is insensitive to the axial stiffness of the cell body. The negative values of strain seen in the distributions are due to lateral contraction that arises from the Poisson effect.

14

8. Results

The embedded neuron model described above provides local strain information within the neuron structure that is inaccessible by current experimental procedures. Therefore, the neuron model serves as a computational microscope that can be used to probe the neuron's response to its mechanical environment under loading. For this study, the collagen gel surrounding the neuron was subjected to grip strains of up to 16%, which corresponds to painful ligament loading (Zhang et al. 2016). The axial and transverse strain distributions in the neuron are examined for the three different loading conditions shown in Fig. 6. The axial cell-body stiffness is set by Eq. (13) with $t = 30$.

Color maps of the maximum principal strain in the neuron structure for a grip strain of 16% (painful ligament loading) and for 0, 45, and 90 degree loading are plotted in Fig. 8. For all angles of loading, large portions of the neuron experience strains that

(a)

(b)

(c)
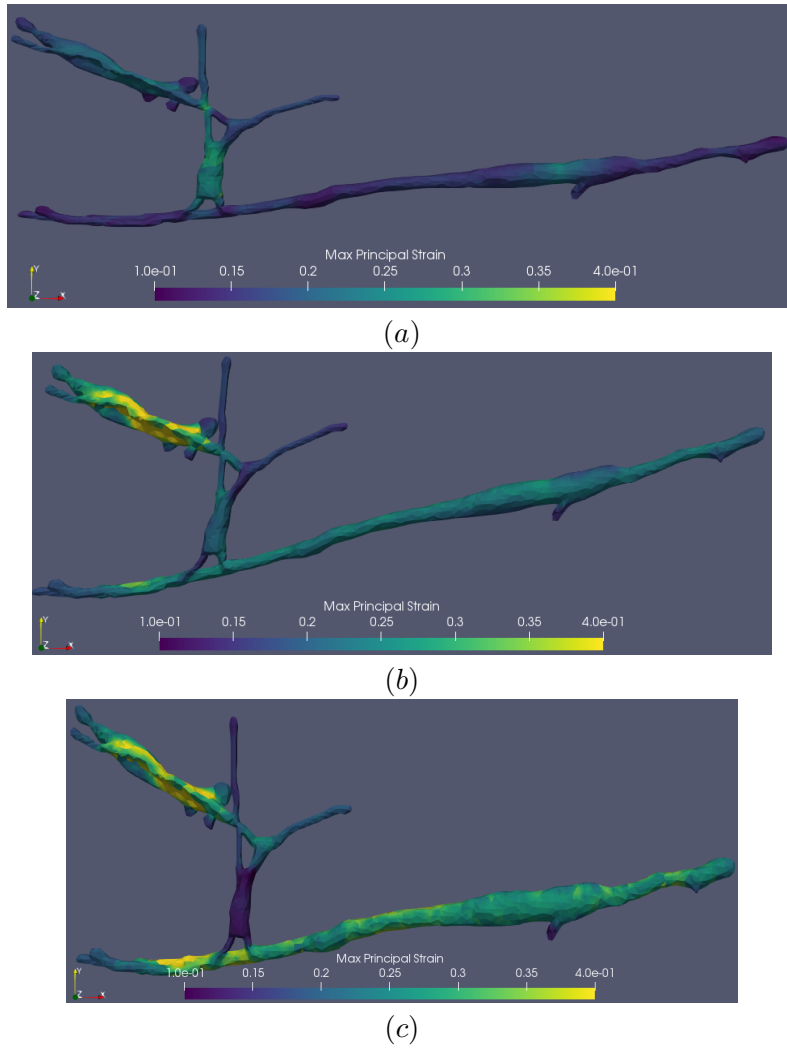
Figure 8. Color maps of MPS in neuron for grip strain of 16% for loading angle of (a) 0, (b) 45, and (c) 90 degrees. The axial stiffness in the cell body is according to Eq. (13) with $t = 30$. The color bar ranges from 10% to 40% MPS.

are greater than the 16% grip strain on the surrounding gel. This indicates that the

15

applied strains on the collagen gel are amplified in the neuron, which could lead to neuronal damage even when the surrounding tissue is moderately loaded.

To gain a more quantitative understanding of the strain distribution in the neuron, the ccdfs of the axial and transverse strains for 10% (non painful ligament loading) and 16% (painful ligament loading) grip strains and loading angles of 0, 45, and 90 degrees are plotted in Fig. 9. The axial and transverse strains are considered separately because the neuron is physically anisotropic (e.g., microtubule bundles are axially aligned).

As observed in Fig. 9, the shape of the strain distributions vary significantly for different applied strains and loading directions. In all cases, the strain magnitude within the neuron is larger for an applied strain of 16%, as expected. Interestingly, beside the axial strain case for 0 degree loading, the same fraction of neuron volume experiences at least the applied strain on the surrounding collagen gel for each loading direction. In the case of axial strain for 0 degree loading, a larger fraction of the neuron volume undergoes an amplification of the applied strain for 16% grip strain than that for 10%. The fraction of neuron volume that experiences at least the applied strain are listed in Table 3 for all cases plotted in Fig. 9.

	axial strain		transverse strains	
Loading Direction	$\epsilon_{\mathrm{grip}} = 0.1$	$\epsilon_{\mathrm{grip}} = 0.16$	$\epsilon_{\mathrm{grip}} = 0.1$	$\epsilon_{\mathrm{grip}} = 0.16$
0 deg.	19%	28%	9%	9%
45 deg.	22%	22%	0.5%	0.3%
90 deg.	13%	13%	67%	67%

Table 3. Fraction of neuron volume that experiences at least the applied strain on surrounding collagen gel for different loading directions.

As seen in Table 3, the applied strain on the collagen gel is amplified in the neuron predominantly along the axial direction for 0 and 45 degree loading and in the transverse direction for 90 degree loading. For 45 degree loading, less than 1% of the neuron volume experiences a transverse strain that is greater than or equal to the applied strain.

Physiologically more important are the tails of the strain distributions which represent the largest strains experienced by the neuron. The strain values corresponding to the largest 10% (by neuron volume) of deformation in the neuron are listed in Table 4. As seen in Table 4, the applied strain is amplified along the axial direction for 0 and

	Largest 10% of axial strain		Largest 10% of transverse strain	
Loading Direction	$\epsilon_{\mathrm{grip}} = 0.1$	$\epsilon_{\mathrm{grip}} = 0.16$	$\epsilon_{\mathrm{grip}} = 0.1$	$\epsilon_{\mathrm{grip}} = 0.16$
0 deg.	0.11	0.19	0.04	0.06
45 deg.	0.16	0.27	0.06	0.10
90 deg.	0.05	0.09	0.22	0.37

Table 4. Strain values corresponding to the largest 10% of deformation in the neuron.

45 degree loading and the transverse direction for 90 degree loading. Of these cases, the largest and smallest amplifications arise for 90 and 0 degree loading, respectively. When the collagen gel is loaded at 90 degrees, the largest axon in the neuron lies perpendicular to the loading direction giving rise to a relatively large deformation in the neuron. On the other hand, when the collagen gel is loaded at 0 degrees, the largest axon in the neuron lies nearly parallel to the loading direction preventing excessive deformation in the neuron.

9. Discussion

The results in Section 8 illustrate that the strain distribution (ccdf) in the neuron structure, and hence strain amplification, is most strongly influenced by the configuration of the neuron with respect to the loading direction. The strong dependence of the strain distribution on loading configuration reflects the anisotropic nature of the embedded neuron structure, where the axial stiffness is more than one order of magnitude greater than the transverse stiffness. Relative to the stiffness of the surrounding collagen gel, the axial stiffness of the neuron is larger while the transverse stiffness of the neuron is smaller. Due to the complex geometry of the embedded neuron structure studied above, the neuron structure is exposed to both transverse and axial components of loading. The spread of the ccdfs reflect the range of tranverse and axial loads that different regions within the neuron structure is exposed to.

[Sijia, Beth, Victor B.: How representative is this one neuron configuration that we study? Can we extrapolate these results to other studies?]

As mentioned above, the spread in the strain distributions reflect the complex geometry of the neuron structure. Of the three loading angles considered, the neuron structure is loaded most uniformly at 45 degrees as reflected by the relatively narrow spread of its strain distribution. The wider spread in the strain distributions for 0 and 90 degree loading is due to the existence of neurons in the structure that lie nearly parallel to the 0 degree and 90 degree axis. As a result, when the gel is loaded at either 0 or 90 degrees, the neuron structure will be exposed to both extremes of nearly pure transverse and axial loadings.

Physiologically most important is the right tail of the distributions, which corresponds to the maximum strain experienced in the neuron structure. Of the cases considered, the largest strain amplification in the neuron structure is observed when the gel is loaded at 90 degrees. As seen in Table 3, 9.7% and 14% of the neuron structure experiences a three times or more strain amplification for non painful and painful ligament loading, respectively. In comparison, 0.2% and 0% of the neuron structure experiences a three times or more strain amplification for 0 and 45 degree loading, respectively. The volume fraction that experiences a two times or more strain amplification for the 0 and 45 degree loading cases is still less than the volume fraction experiencing three times or more strain amplification in the 90 degree loading case.

Of the three loading configurations considered, the 90 degree loading case is most susceptible to neuronal damage during ligament loading as reflected by the large average and long tail of its distribution. In the cases of the 0 and 45 degree loading, the strain distribution for 45 degrees has a larger average while that for 0 degrees has a longer tail. Therefore, whether the 0 or 45 degree loading case is more susceptible to neuron injury depends on the damage threshold of the neuron. For example, if the damage threshold for the neuron is three times the applied load on the gel, then the 0 degree loading case will be more susceptible to neuronal damage due to the longer tail in its distribution.

10. Conclusion [Remove]

In this paper we developed a multi-scale model of a neuron structure that is embedded in a collagen gel to examine the local strain response that arises when innervated collagenous tissue is deformed. The model presented in this work provides local strain

information that is inaccessible by current experimental techniques, thereby serving as a computational microscope. Such local strain information was used to examine the embedded neuron structure's susceptibility to injury, which provides insights about the cause of pain when an innervated ligament is excessively loaded.

The embedded neuron geometry for this model was generated from confocal images to incorporate the complex structure of the neuron. The realistic representation of the embedded neuron structure enables us to extend our findings to actual physiological environments. The distribution of local strains that arise in the neuron structure were examined for different cell body stiffnesses in the neuron structure and loading configurations on the surrounding collagen gel. We showed that the local-strain distribution depends only weakly on the cell body stiffness, while varying significantly for different loading configurations. The strong dependence on loading configuration is a consequence of the anisotropic nature of the neuron, which has an axial stiffness that is one order greater that its transverse stiffness.

The spread in the strain distributions reflects the range of deformation that arises within the neuron structure due to its complex geometry; regions within the neuron structure experience different degrees of transverse and axial loading. We showed that transverse loading of the neuron gave rise to local-strain amplification, while axial loading gave rise to local strains in the neuron that are smaller than the applied load on the surrounding gel. Consequently, a larger average local-strain amplification corresponds to a larger degree of transverse loading in the neuron structure.

In this work, we considered loading along the 0, 45, and 90 degree axis, which are illustrated in Fig. ??. As the loading angle varied from 0 to 90 degrees, the volume fraction of the neuron structure experiencing transverse loading increased, as reflected by the increasing average local-strain amplification. The neuron structure was loaded most uniformly at 45 degrees, as reflected by the relatively narrow spread of the strain distribution. At 0 and 90 degree loading, the neuron structure experiences the extremes of both nearly pure transverse and axial loading due to the existence of neurons that are nearly parallel to the 0 and 90 degree axes. Consequently, the spread in the distribution for 0 and 90 degree loading are wider.

The right tail of the distributions, which represent the maximum strain experienced in the neuron structure, was found to be the largest for the 90 degree loading case - 9.7% and 14% of the neuron structure experienced at least a three times local strain amplification for non painful and painful ligament loading, respectively. In contrast, 0.2% and 0% of the neuron structure experienced the same strain amplification for the 0 and 45 degree loading cases, respectively.

Overall, the 90 degree loading configuration was found to be most susceptible to neuronal injury because of the large average and long tail of its distribution. In the other cases, the strain distribution for 45 degree loading has a larger average while that for 0 degree loading has a longer tail. Therefore, whether the 0 or 45 degree loading configurations are more susceptible to neuronal injury depends on the strain threshold for damage on the neuron. For example, if the damage threshold is more than three times the applied strain, the 0 degree loading configuration is more susceptible to neuronal injury because of the longer tail in its distribution.

This study has provided initial insights about the local-strain amplifications that arise in the embedded neuron structure during deformation to the surrounding collagenous tissue. These findings support the hypothesis that embedded neurons can be damaged even when the surrounding collagenous tissue is moderately loaded. Additional insights on the cause of neuron damage during ligamentous matrix loading can be uncovered by extending this study to a larger number of embedded neurons. The

technology presented in this work can be readily extended to such a system.

References

2017. Simmetrix. Available from: http://www.simmetrix.com.

Barocas VH. 2007. Multiscale, Structure-Based Modeling for the Elastic Mechanical Behavior of Arterial Walls. Journal of Biomechanical Engineering. 129(4):611–8.

Bonet J, Burton AJ. 1998. A simple orthotropic, transversely isotropic hyperelastic constitutive equation for large strain computations. Computer Methods in Applied Mechanics and Engineering. 162(1-4):151–164.

Bonet J, Wood D R. 2008. Nonlinear Continuum Mechanics for Finite Element Analysis. 2nd ed. Cambridge University Press.

Chandran PL, Barocas VH. 2007. Deterministic Material-Based Averaging Theory Model of Collagen Gel Micromechanics. Journal of Biomechanical Engineering. 129(2):137–11.

Delalondre F, Smith C, Shephard MS. 2010. Collaborative software infrastructure for adaptive multiple model simulation. Computer Methods in Applied Mechanics and Engineering. 199(21-22):1352–1370.

Dutov P, Antipova O, Varma S, Orgel JPRO, Schieber JD. 2016. Measurement of Elastic Modulus of Collagen Type I Single Fiber. Plos One. 11(1).

Eppell SJ, Smith BN, Kahn H, Ballarini R. 2006. Nano measurements with micro-devices: mechanical properties of hydrated collagen fibrils. Journal of The Royal Society Interface. 3(6):117–121.

Fletcher DA, Mullins RD. 2010. Cell mechanics and the cytoskeleton. Nature.

Hashin Z. 1962. The elastic moduli of heterogeneous materials. Journal of Applied Mechanics. 29(1):143–150.

Humphrey JD, Rajagopal KR. 2002. A constrained mixture model for growth and remodeling of soft tissues. Mathematical models and methods . . . . 12(03):407–430.

Klaas O, Beall MW, Shephard MS. 2013. Construction of models and meshes of heterogeneous material microstructures from image data. Image-Based Geometric Modeling and Mesh Generation. 3:171–193.

Klass Ottmar SMS Beall Mark W. 2014. Generation of geometric models and meshes from segmented data. In: Proc. NAFEMS Americas Conference 2014.

Lai VK, Hadi MF, Tranquillo RT, Barocas VH. 2013. A Multiscale Approach to Modeling the Passive Mechanical Contribution of Cells in Tissues. Journal of Biomechanical Engineering. 135(7):071007.

Lai VK, Lake SP, Frey CR, Tranquillo RT, Barocas VH. 2012. Mechanical Behavior of Collagen-Fibrin Co-Gels Reflects Transition From Series to Parallel Interactions With Increasing Collagen Content. Journal of Biomechanical Engineering. 134(1):011004–19.

Lake SP, Hadi MF, Lai VK, Barocas VH. 2012. Mechanics of a Fiber Network Within a Non-Fibrillar Matrix: Model and Comparison with Collagen-Agarose Co-gels. Annals of Biomedical Engineering. 40(10):2111–2121.

Lindström SB, Kulachenko A, Jawerth LM, Vader DA. 2013. Finite-strain, finite-size mechanics of rigidly cross-linked biopolymer networks. Soft Matter. 9(30):7302–12.

Lorensen W. 1987. Marching cubes: A high resolution 3D surface construction algorithm. ACM Siggraph Computer Graphics.

Marquez JP, Genin GM, Pryse KM, Elson EL. 2006. Cellular and Matrix Contributions to Tissue Construct Stiffness Increase with Cellular Concentration. Annals of Biomedical Engineering. 34(9):1475–1482.

Peter SJ, Mofrad MRK. 2012. Computational Modeling of Axonal Microtubule Bundles under Tension. Biophysical Journal. 102(4):749–757.

Quinn KP, Winkelstein BA. 2008. Altered collagen fiber kinematics define the onset of localized ligament damage during loading. Journal of Applied Physiology. 105(6):1881–1888.

Quinn KP, Winkelstein BA. 2009. Vector correlation technique for pixel-wise detection of collagen fiber realignment during injurious tensile loading. Journal of Biomedical Optics. 14(5):054010–10.

Schneider CA, Rasband WS, Eliceiri KW. 2012. NIH Image to ImageJ: 25 years of image

analysis. Nature Methods. 9(7):671–675.

Shephard MS. 2000. Meshing environment for geometry-based analysis. International Journal for Numerical Methods in Engineering. 47:169–190.

Simon M, Dokukin M, Kalaparthi V, Spedden E, Sokolov I, Staii C. 2016. Load Rate and Temperature Dependent Mechanical Properties of the Cortical Neuron and Its Pericellular Layer Measured by Atomic Force Microscopy. Langmuir. 32(4):1111–1119.

Stylianopoulos T, Barocas VH. 2007. Volume-averaging theory for the study of the mechanics of collagen networks. Computer Methods in Applied Mechanics and Engineering. 196(31-32):2981–2990.

Svensson RB, Hassenkam T, Hansen P, Magnusson SP. 2010. Viscoelastic behavior of discrete human collagen fibrils. Journal of the Mechanical Behavior of Biomedical Materials. 3(1):112–115.

Tower TT, Neidert MR, Tranquillo RT. 2002. Fiber alignment imaging during mechanical testing of soft tissues. Annals of Biomedical Engineering. 30(10):1221–1233.

Vader D, Kabla A, Weitz D, Mahadevan L. 2009. Strain-Induced Alignment in Collagen Gels. Plos One. 4(6):e5902–12.

Whitaker S. 1999. The method of volume averaging. Springer.

Zhang S, Cao X, Stablow AM, Shenoy VB, Winkelstein BA. 2016. Tissue Strain Reorganizes Collagen With a Switchlike Response That Regulates Neuronal Extracellular Signal-Regulated Kinase Phosphorylation In Vitro: Implications for Ligamentous Injury and Mechanotransduction. Journal of Biomechanical Engineering. 138(2):021013–12.

Appendix A: Derivation of P_2 from α and δ of the QPLI method

Consider a distribution of orientation θ for pixel i as

$$p_i(\theta) = q_i + r_i \cos^2(\theta - \alpha_i) \ \text{ for } \ \theta \in (0, \pi), \tag{1}$$

where α_i is the alignment measured at pixel i by the QPLI method and q_i and r_i are constants for the ith pixel. Applying the normalization

$$\int_0^\pi p_i(\theta)d\theta = 1, \tag{2}$$

a relationship between q_i and r_i is obtained:

$$\pi q_i + \frac{\pi}{2}r_i = 1. \tag{3}$$

Using the relationship in Eq. (3), Eq. (1) can be rewritten as

$$p_i(\theta) = q_i + \frac{2}{\pi}(1 - \pi q_i)\cos^2(\theta - \alpha_i) \tag{4}$$

The orientation tensor for each pixel can be written in terms of $p_i(\theta)$ as

$$\boldsymbol{A}^i = \begin{bmatrix} \int_0^\pi p_i(\theta)\cos^2(\theta)d\theta & \int_0^\pi p_i(\theta)\sin(\theta)\cos(\theta)d\theta \\ \int_0^\pi p_i(\theta)\sin(\theta)\cos(\theta)d\theta & \int_0^\pi p_i(\theta)\sin^2(\theta)d\theta \end{bmatrix} = \frac{1 - \pi q_i}{4}\begin{bmatrix} \cos(2\alpha_i) & \sin(2\alpha_i) \\ \sin(2\alpha_i) & -\cos(2\alpha_i) \end{bmatrix}, \tag{5}$$

where the eigenvalues of $\boldsymbol{A}^i$ are

$$\lambda_1 = \frac{1 + \pi q_i}{4} \quad \text{and} \quad \lambda_2 = \frac{3 - \pi q_i}{4}. \tag{6}$$

The retardation at each pixel, δ_i, can be calculated from the eigenvalues by

$$\delta_i = |\lambda_2 - \lambda_1| = \frac{1 - \pi q_i}{2}. \tag{7}$$

From Eq. (7), the constant q_i can be written in terms of the retardation as

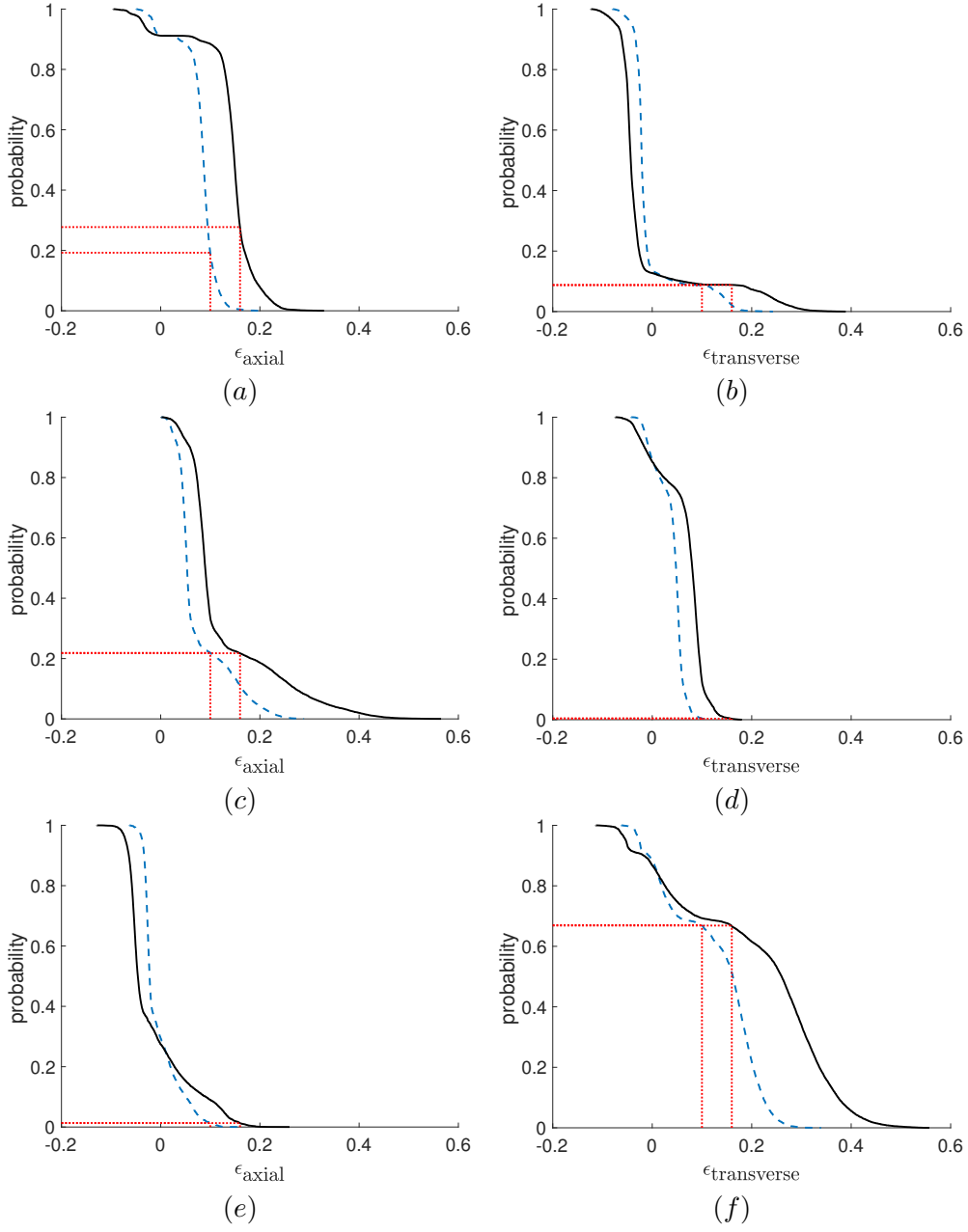$$q_i = \frac{1}{\pi}(1 - 2\delta_i), \tag{8}$$

and the distribution at pixel i from Eq. (4) can be rewritten as

$$p_i(\theta) = \frac{1 - 2\delta_i}{\pi} + \frac{4\delta_i}{\pi} \cos^2(\theta - \alpha_i). \tag{9}$$

The distribution of orientation θ for the entire image is simply the average over the distribution of each pixel

$$p(\theta) = \frac{1}{N} \sum_{i=1}^{N} p_i(\theta) = \frac{1}{N} \sum_{i=1}^{N} \left[\frac{1 - 2\delta_i}{\pi} + \frac{4\delta_i}{\pi} \cos^2(\theta - \alpha_i) \right], \tag{10}$$

which is the equation presented in Eq. (11).

Figure 9. Complementary cumulative distribution functions for axial (left column) and transverse (right column) strains in neuron for 0 (top row), 45 (middle row), and 90 (bottom row) degree loading. Distributions for 10% (blue dashed line) and 16% (black solid line) grip strains are plotted for all loading directions. The dotted red lines indicate the fraction of neuron volume that experience a strain of at least 10% and 16% when intersecting with the dashed blue and solid black lines, respectively.